European Geothermal Congress 2016
Strasbourg, France, 19-24 Sept 2016

Time-lapse seismic imaging of the Reykjanes geothermal reservoir

Cornelis Weemstra[1], Anne Obermann[2], Arie Verdel[3], Bob Paap[3], Hanna Blanck[4], Egill Árni Guðnason[4], Gylfi Páll Hersir[4], Philippe Jousset[5], Ómar Sigurðsson[6]

[1] Delft University of Technology, Delft, The Netherlands

[2] ETH, Zürich, Switzerland

[3] TNO, Utrecht, The Netherlands

[4] ISOR, Reykjavik, Iceland

[5] GFZ, Potsdam, Germany

[6] HS Orka, Reykjanesbær, Iceland

kweemstra@gmail.com

Keywords: surface waves, seismic interferometry, seismic monitoring, Reykjanes

ABSTRACT

We report on the results obtained from a dense seismic deployment over a geothermal reservoir located on the tip of the Reykjanes peninsula, SW Iceland. The available seismic stations have continuously recorded the ambient-seismic wave field between April 2014 and August 2015. Using seismic interferometry (SI), seismic responses were generated between these receivers. SI allows one to turn one receiver of a receiver pair into a so-called 'virtual source', whose response is then retrieved by the other receiver. The retrieved virtual-source response approximates the medium's Green's function between the two receiver locations. For the ambient-seismic recordings used in this study, virtual-source retrieval involves simple time-averaging of the crosscorrelations between these recordings. The virtual-source responses were retrieved in a time-lapse manner. The temporal variation of the 'coda' of these virtual-source responses has been evaluated, where the term coda refers to the later arriving, multiply scattered waves. The multiple scattering implies that these waves have sampled the subsurface very densely and hence have become highly sensitive to tiny mechanical and structural changes in that subsurface. We did not find a clear relation between the temporal variation of the coda waves and the injection/extraction rates of the geothermal reservoir.

1. INTRODUCTION

Despite the fact that early foundations have been laid a long time ago by seismologists such as Aki (1957) and Claerbout (1968), SI gained most of its popularity over the last decade. By now, many applications have arisen that exploit the technique to infer characteristics of the subsurface (e.g., Shapiro *et al.*, 2005; Sens-Schönfelder and Wegler, 2011). The technique is also successfully applied to other media, such as, among others, the sun (Duvall *et al.*, 1993), the oceans (Roux and Fink, 2003; Woolfe *et al.*, 2015), buildings (Snieder and Şafak, 2006; Kohler *et al.*, 2007), and the atmosphere (Haney, 2009; Fricke *et al.*, 2014).

1.1 Seismic interferometry

SI refers to the principle of generating new seismic responses from existing recordings. Considering a pair of receivers, SI allows one to turn one of these receivers into a so-called 'virtual source', whose response is then retrieved by the other receiver. Applied to the real Earth, a new response is generally obtained by simple crosscorrelation of sufficiently long recordings of ambient-seismic noise at the two receiver locations (e.g., Campillo and Paul, 2003; Draganov *et al.*, 2009; Zhan *et al.*, 2010). Using controlled sources, an additional summation of crosscorrelations over the available source positions is required (e.g., Schuster *et al.*, 2004; Bakulin and Calvert, 2006).

Responses retrieved through SI can be related to the Green's function of the medium under specific conditions (Wapenaar and Fokkema, 2006; Halliday and Curtis, 2008). Over the last decade, numerous applications have emerged that rely on this explicit relation. The most notable probably being the extraction of receiver-receiver phase and/or group velocities from the retrieved interferometric surface-wave responses. The extracted velocities often serve as input parameters for tomographic inverse problems (e.g., Shapiro *et al.*, 2005).

Up to date, predominantly surface-wave responses are retrieved through the application of SI. This can be attributed to the fact that ambient-seismic vibrations on Earth are dominated by surface waves. The most energetic source of that type of waves are the oceans (McNamara and Buland, 2004; Kedar *et al.*, 2008). In particular, interaction of ocean gravity waves with coinciding periods traveling in opposite directions results in an effective excitation of the solid Earth (Longuet-Higgins, 1950; Hasselmann, 1963). Ambient vibrations resulting from the coupling of the ocean with the solid Earth, are referred to as 'microseisms' and the continuous ocean-bottom excitation ensures that they are ever-present. Microseisms carry most energy around 0.15 Hz (e.g., McNamara and Buland, 2004), but their spectral content extends up to 1.0 Hz in coastal regions.

1.2 Coda-wave interferometry

Another application of SI involves the monitoring of tiny changes in a medium by means of the so-called 'coda' of the retrieved virtual-source responses (e.g., Sens-Schönfelder and Wegler, 2006). The term coda refers to later-arriving multiply scattered waves. These multiply scattered waves are more sensitive to structural changes in the medium and are therefore more suited for seismic monitoring than the direct arrival. Using the seismic coda to infer changes in the medium is generally referred to as 'coda-wave interferometry' (Snieder *et al.*, 2002). The ever-present ambient vibrations ensure continuous retrieval of virtual-source responses and hence obviate the need for expensive and disturbing repetitive controlled sources. The continuous nature of the virtual-source responses also implies that these do not suffer from a lack of repeatability that responses obtained from natural sources, such as earthquakes, might exhibit (e.g., Poupinet *et al.*, 1984). It is useful to note that the condition that the medium is illuminated uniformly from all angles, which is a requirement for accurate Green's function retrieval (Tsai, 2009; Weaver *et al.*, 2009), can be relaxed for monitoring purposes (Hadziioannou *et al.*, 2009). These authors demonstrate that a stable background wave field suffices to infer tiny mechanical and structural medium changes from the coda. Seismic monitoring using coda-wave interferometry has been applied successfully on various scales (e.g., Stähler *et al.*, 2011; Obermann *et al.*, 2014) and in a variety of environments (Sens-Schönfelder and Wegler, 2011).

Recently, the use of SI in a geothermal context has received considerable attention. In 2014, the cumulative global geothermal capacity reached over 12 GW; this is expected to rise to over 16 GW in 2020 (International Energy Agency (IEA), 2015). Two types of geothermal systems can be distinguished. First, 'hydrothermal systems', which can be found at tectonic boundaries and/or in volcanic areas, are naturally profitable because they exploit existent aquifers. These systems account for the bulk of the global geothermal capacity. Second, 'enhanced geothermal systems' (EGS) aim to utilize thermal energy in the crystalline basement. Enhancement of the limited permeability of the basement generally involves the injection of fluids into the rock mass at a high pressure, which causes it to fracture. It is mainly this type of geothermal system that has recently been probed using SI (Hillers *et al.*, 2015; Lehujeur *et al.*, 2015; Obermann *et al.*, 2015).

The potential of SI for the purpose of seismic monitoring lies in the effect of aseismic transient subsurface deformation on the coda of the retrieved virtual-source responses. For example, using an array of 9 seismic stations, Obermann *et al.* (2015) observe a significant loss of waveform coherence that can be constrained to the injection location at the St. Gallen geothermal site. Hillers *et al.* (2015) observe an aseismic transient deformation induced by the 2006 EGS stimulation underneath the city of Basel, Switzerland.

As mentioned above, ideally the background wave field is stable with time. If this is not the case, loss of waveform coherence and/or a change in arrival time of the seismic coda may be due to change in the illumination pattern, instead of caused by a change in the medium. Using cultural noise, Lehujeur *et al.* (2015) show that it may therefore be beneficial to select specific time windows during which the background wave field is most stable.

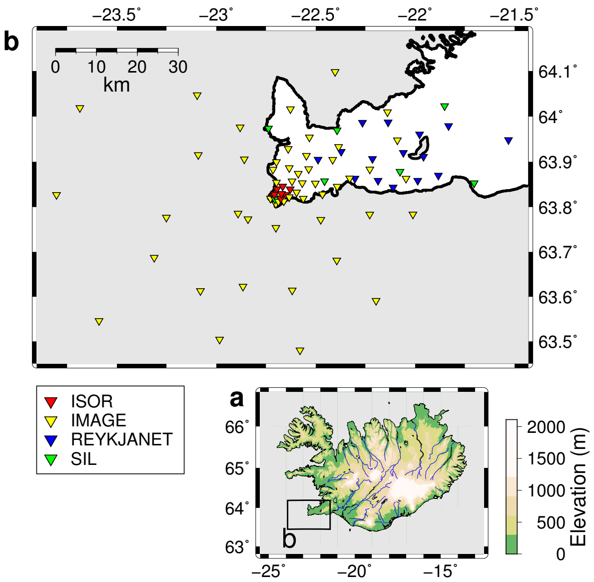

Figure 1: The location of the RARR (a) and its station configuration (b).

In this study we use ambient-seismic noise recorded by a subset of the Reykjanes Array (RARR) (Figure 1). The bulk of the stations of the RARR or deployed in the context of IMAGE (Integrated Methods for Advanced Geothermal Exploration). We focus on the southwestern tip of the Reykjanes peninsula where the Mid-Atlantic ridge comes ashore. The Reykjanes geothermal system (RGS) is located right on this tip. This system has been exploited on a small scale for decades, but in 2006 a new power plant was installed. Since then, approximately 100 MW of electricity is produced annually. The associated increased production rate has caused drastic changes in reservoir conditions, in particular a considerable drop of the pressure in the reservoir (Axelsson *et al.*, 2015). In this study we assess the capability of SI to infer tiny mechanical and structural changes in the RGS.

In the following section, we introduce the theory underlying SI and coda-wave interferometry. Subsequently, we introduce the RARR and its data. We then present the results obtained so far and finish with a discussion.

2. THEORY

Consider two seismic stations: a first station, S_i, located at $\boldsymbol{x}_i$ and a second station S_j, located at $\boldsymbol{x}_j$. We denote the recordings of ambient vertical particle velocity at $\boldsymbol{x}_i$ and $\boldsymbol{x}_j$ by v_i and v_j, respectively. The crosscorrelation C_{ij}^T of these ambient recordings is then given by,

$$C_{ij}^T(t) \equiv \frac{1}{2T}\int_{-T}^{T} v_i(\tau)v_j(\tau+t)d\tau, \qquad [1]$$

where t is time, τ is integration time and where we have normalized with respect to the length of the employed crosscorrelation window, i.e., T. We assume the length of this crosscorrelation window to be sufficiently long with respect to the longest period within the frequency range of interest, i.e., $T \gg 1/\omega$, with ω the angular frequency. Note that signal that is recorded by S_i prior to the time of recording by S_j will peak at positive time, whereas signal passing $\boldsymbol{x}_j$ before $\boldsymbol{x}_i$ will peak at negative time.

In case several (noise) sources are acting simultaneously within a period of length T, spurious travel-time delays arise due to constructive interference of signal coming from different sources (Snieder *et al.*, 2008; Weemstra *et al.*, 2014). Cancellation of these spurious arrivals is a requirement for the successful retrieval of interferometric receiver-receiver signal and can be achieved through ensemble averaging (Wapenaar and Fokkema, 2006; Hanasoge, 2013). In practice, ensemble averaging is replaced by averaging over a large number of crosscorrelation windows (e.g., Weemstra *et al.*, 2013). We define the ensemble-averaged crosscorrelation as $C_{ij}(t) \equiv \langle C_{ij}^T(t)\rangle$. The ensemble-averaged crosscorrelation $C_{ij}(t)$ can be related to the Green's function between $\boldsymbol{x}_i$ and $\boldsymbol{x}_j$ if (i) the noise sources illuminate the station couple uniformly from all angles and (ii) the medium is lossless. Under these assumptions the ensemble-averaged crosscorrelation will be proportional to the Green's function and its time-reversed version, convolved with the autocorrelation of the (noise) sources (Wapenaar and Fokkema, 2006), i.e.,

$$C_{ij}(t) \propto \left[G\left(\boldsymbol{x}_j,\boldsymbol{x}_i,t\right) + G\left(\boldsymbol{x}_j,\boldsymbol{x}_i,-t\right)\right] * P(t) \qquad [2]$$

where the in-line asterisk $*$ denotes temporal convolution and where $P(t)$ denotes the autocorrelation of the (noise) sources.

In practice, equation [2] is often not exact and at best an estimate of the Green's function and its time-reversed version is obtained. The estimate of $G\left(\boldsymbol{x}_j,\boldsymbol{x}_i,t\right)$ is generally referred to as 'the causal part' of the ensemble-averaged crosscorrelation, whereas the estimate of $G\left(\boldsymbol{x}_j,\boldsymbol{x}_i,-t\right)$ is generally referred as the 'anti-causal part' of $C_{ij}(t)$. The fact that equation [2] is often not exact may be due to a number of reasons. The most notable probably being the absence of a uniform illumination pattern (Stehly *et al.*, 2006; Mulargia, 2012; Boschi and Weemstra, 2015). In the case of surface waves, the resulting deviation of the surface-wave part of $C_{ij}\left(t\right)$ from the actual, correct surface-wave response, may lead to inaccurate phase and/or group velocity measurements (Tsai, 2009; Weaver *et al.*, 2009). Furthermore, the deviations associated with the non-uniform illumination pattern may be aggravated by cross-modal terms (Halliday and Curtis, 2008; Kimman and Trampert, 2010). In this work we make the assumption that a single surface-wave mode dominates the surface-wave field. In that case, cross-modal terms will be absent.

In the presence of heterogeneity, the Green's function (and hence the ensemble-averaged crosscorrelation) will contain both a direct arrival and scattered arrivals (Boschi and Weemstra, 2015). In this work we will focus on the multiply scattered arrivals in the retrieved virtual-source responses, i.e., the coda. To that end, we define for each receiver pair ij a reference ensemble-averaged crosscorrelation (henceforth 'reference crosscorrelation'), $C_{ij}^{(ref)}$, and a time-lapse ensemble-averaged crosscorrelation (henceforth 'lapse crosscorrelation'), $C_{ij}^{(lapse)}$. Lapse crosscorrelations are obtained on a daily basis by stacking individual crosscorrelations (obtained through the implementation of equation [1]) over a limited period of time. This period needs to be long enough to ensure stable lapse crosscorrelations, which in practice depends on the frequency of interest and the stability of the illumination pattern. Subsequently, we compare the coda of the lapse crosscorrelation against the coda of the reference crosscorrelation.

Changes in the coda over time can be quantified using the stretching technique (Lobkis and Weaver, 2003; Sens-Schönfelder and Wegler, 2006). This technique exploits the fact that a spatially homogeneous velocity variation in the medium (with respect to the reference medium) will stretch or compress the waveform in time. For each receiver pair, we therefore compute the 'correlation coefficient', CC, between the coda of the lapse crosscorrelation and the coda of the reference crosscorrelation. The correlation coefficient is computed for a set of values $\epsilon = \delta v/v$ (henceforth referred to as the stretching parameter), which compress ($\epsilon > 0$) or stretch ($\epsilon < 0$) the time-axis, i.e.,

$$CC\left(\epsilon\right) = \frac{\displaystyle\int_{t_1}^{t_2} C_{ij}^{(lapse)}\left[t\left(1-\epsilon\right)\right] C_{ij}^{(ref)}\left[t\right] \mathrm{d}t}{\sqrt{\displaystyle\int_{t_1}^{t_2}\left(C_{ij}^{(lapse)}\right)^2\left[t\left(1-\epsilon\right)\right]\mathrm{d}t}\ \sqrt{\displaystyle\int_{t_1}^{t_2}\left(C_{ij}^{(ref)}\right)^2\left[t\right]\mathrm{d}t}}, \qquad [3]$$

where t_1 and t_2 are the start and end-time of the coda window that has been used. The maximum of $CC(\epsilon)$ we denote by CC_{ij} and the value of ϵ for which CC reaches this maximum we denote by ϵ_{ij}, i.e., $CC_{ij} \equiv CC(\epsilon_{ij})$. Note that a positive value of ϵ_{ij} implies that the coda of the lapse crosscorrelation arrived earlier than the coda of the reference crosscorrelation. This suggests an increase of velocity in a region of the medium during the period over which individual C_{ij}^{T} were averaged to obtain $C_{ij}^{(lapse)}$.

3. DATA CHARACTERISTICS & PROCESSING

The RARR consists of a total of 83 seismic stations and was located on and around the Reykjanes peninsula (Figure 1). It is a composite array formed by using stations from four different seismic networks/deployments. Three of these networks are currently still running. Of the 83 stations, 53 stations were deployed in the context of IMAGE (yellow), which included 23 ocean bottom seismometers (OBSs). Another 15 stations constitute REYKJANET (blue), which is operated by the Iceland GeoSurvey (ISOR) on behalf of the institute of geophysics of the Czech acadamy of sciences (CAS). The deployment referred to as 'ISOR' (red) consists of 8 stations and is also operated by ISOR, but on behalf of HS Orka, the operator of the geothermal power plant on the tip of Reykjanes. Finally, 7 stations are part of the SIL network (green) and are operated by the Icelandic meteorological office (MET office).

3.1 Data characteristics

The temporal data coverage of all stations of the RARR is presented in Figure 2. Because the stations deployed in the context of IMAGE ran from the beginning of April 2014 till September 2015, we restrict our analysis to this period (the other networks are still running). A number of stations on the tip of the Reykjanes peninsula were selected for the application of coda-wave interferometry. These stations were located either on top or close to the RGS. Most of the selected stations have been recording quasi-continuously. Since these stations were part of different networks, they were equipped with different instruments. To prevent relative (time-varying) time shifts of the time-averaged crosscorrelations, each station's instrument response has therefore been removed prior to crosscorrelation.

Figure 3 presents a spectrogram computed from the ambient recordings by station EIN. This spectrogram is representative for all recordings by the RARR and a number of conclusions can be drawn regarding the ambient-seismic wave field on and around Reykjanes. First, during summer (May - August) the captured microseisms are less energetic than during fall and winter. Second, the ambient-seismic field is, on average, most powerful at a frequency of about 0.2 Hz. In winter, however, this frequency is slightly lower, whereas in summer it is slightly higher. Third, especially during fall and winter, multi-day burst of energy can be observed. At lower frequencies, these bursts of ambient-seismic energy are most likely the result of distant (storm-induced) ocean swell coupling into the solid Earth (Longuet-Higgins, 1950). The bathymetry of the North Atlantic Ocean makes that region particularly fit for efficient coupling (Stehly *et al.*, 2006; Kedar *et al.*, 2008). At higher frequencies (>0.25 Hz) the seismic energy generally shows a stronger correlation with local ocean wave activity (Bromirski *et al.*, 2005).

3.2 Data processing

The preprocessing of the data involved (i) decimation of the data to a sampling rate of 10 samples per second, (ii) removal of the instrument response through division of the spectra by the transfer function of the instrument, (iii) cutting of the recordings in time windows of one hour ($T = 3600$ s), (iv) filtering of the data, and (v) removal of time windows containing strong (earthquake) events. The last procedure is required because strong transient events interrupt the (assumed) stability of the background wave field. Events were detected using the energy in a short time window with respect to the energy in long time window lagging this short time window. Such a detection algorithm is generally referred to as an 'sta/lta algorithm', where sta and lta stand for short-term average and long-term average, respectively (e.g., Withers *et al.*, 1998). We computed the short-term average over a period of 16 seconds, whereas the long-term average was computed over a period of 11200 seconds. Furthermore, the lta-window lagged the sta-window by 800 seconds and the sta/lta algorithm advanced through time with increments of 8 seconds. One-hour time windows containing (one or more) sta-window values exceeding a threshold of 6 were discarded.

Despite the applied instrument corrections, it turned out that below 1 Hz the phase of the recordings by the stations of the SIL, ISOR, and REYKJANET networks, was shifted with respect to the actual phase. This inaccuracy was observed upon comparison of these recordings with the recordings by the (broad-band) IMAGE stations. As a consequence, the stability of the coda of lapse crosscorrelations including one (or two) of these stations could not be guaranteed. We have therefore limited ourselves to the stations close to the RGS that were part of the IMAGE seismic network (data represented by black bars in Figure 2). We are currently in the process of correcting the phase of the recordings by the other networks by exploiting the time-symmetry of the retrieved virtual-source responses predicted by equation [2] (e.g., Stehly *et al.*, 2007).

Following the preprocessing, crosscorrelations were computed for each of the selected receiver couples with an overlap of 50% between consecutive time windows. At each discrete frequency, the amplitude spectrum of the hourly recordings was normalized with respect to the average spectral amplitude in a 0.005 Hz range around that frequency. This so-called 'spectral whitening' ensures that the individual C_{ij}^{T} weight equally at each fre-

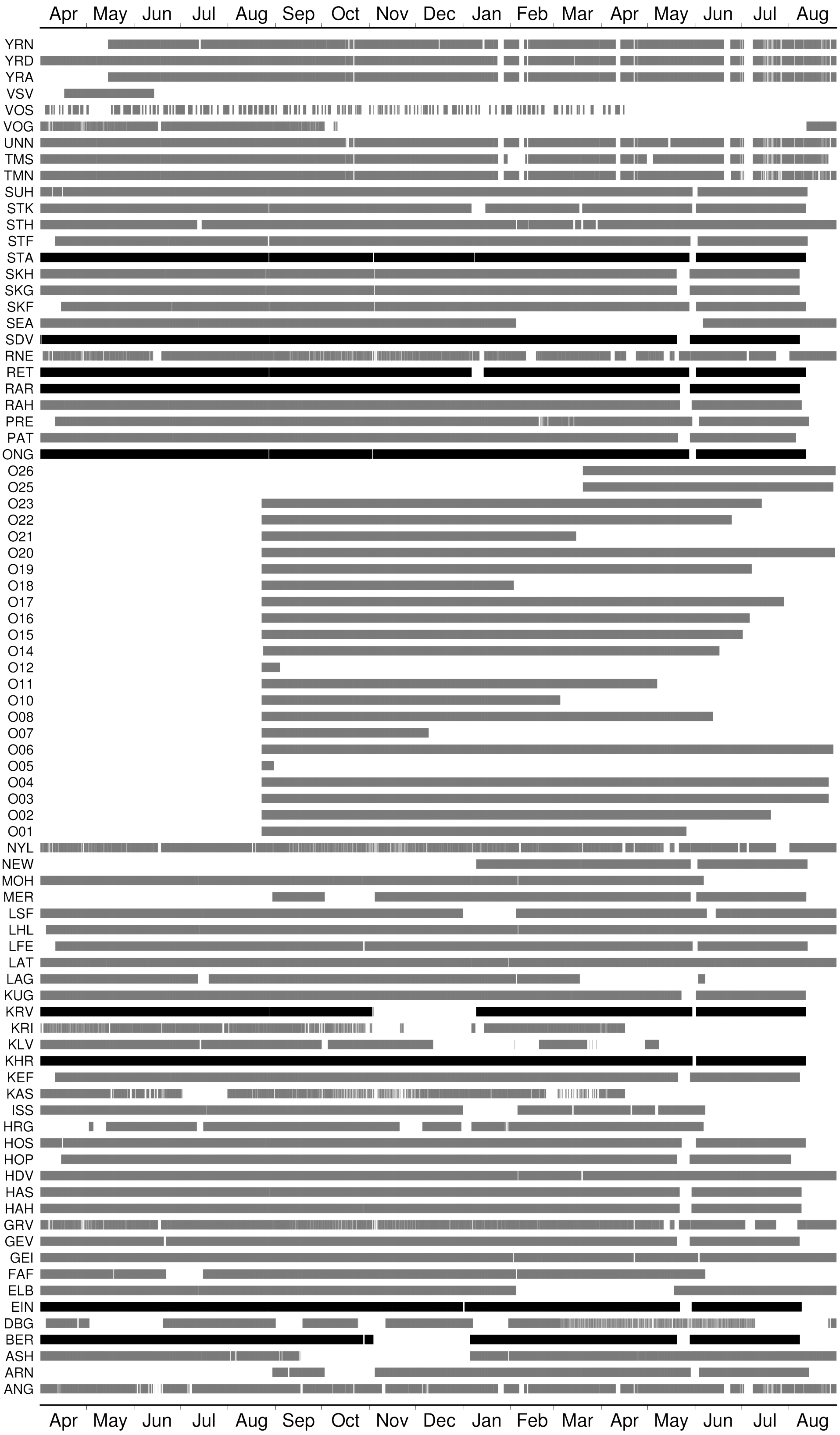

Figure 2: Data availability for each of the stations of the RARR during 2014 and 2015. Black colored bars represent data selected for the application of coda-wave interferometry, whereas the gray colored data has so far not been used in this study. Stations O[01-26] are ocean bottom seismometers.

quency in the ensemble-averaging process (Seats *et al.*, 2012; Weemstra *et al.*, 2014). For each station pair, the reference crosscorrelation was obtained by averaging individual crosscorrelations over the full common recording period. Lapse crosscorrelations were obtained on a daily basis by averaging individual C_{ij}^{T} over a period of 30 days. This implies a temporal resolution of our results of 30 days. Figure 4 depicts the retrieved

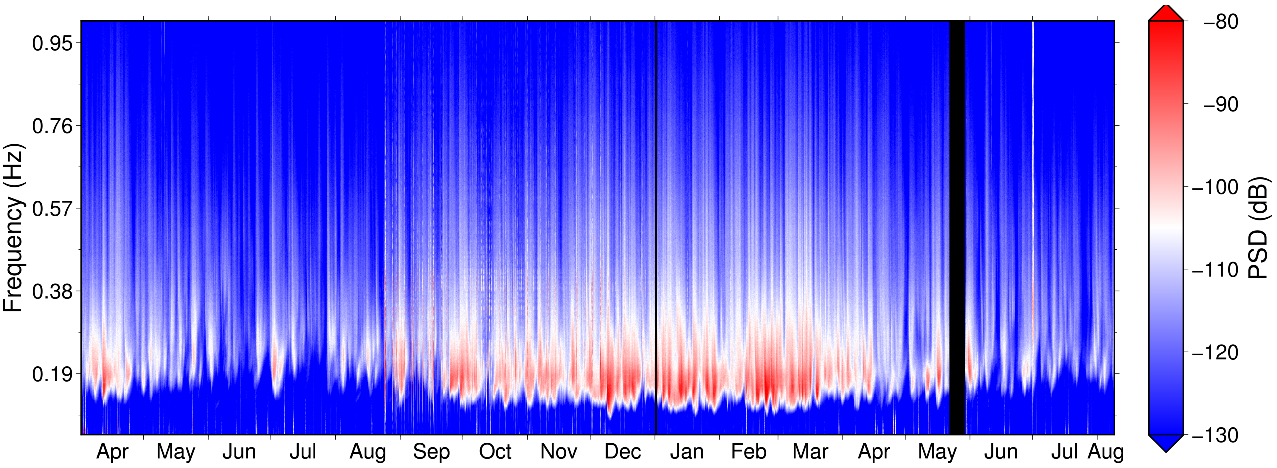

Figure 3: Spectrogram computed from the recordings by station EIN, which is located in the center of the RARR. Power spectra are averaged over four hours and 1.39×10^{-3} Hz.

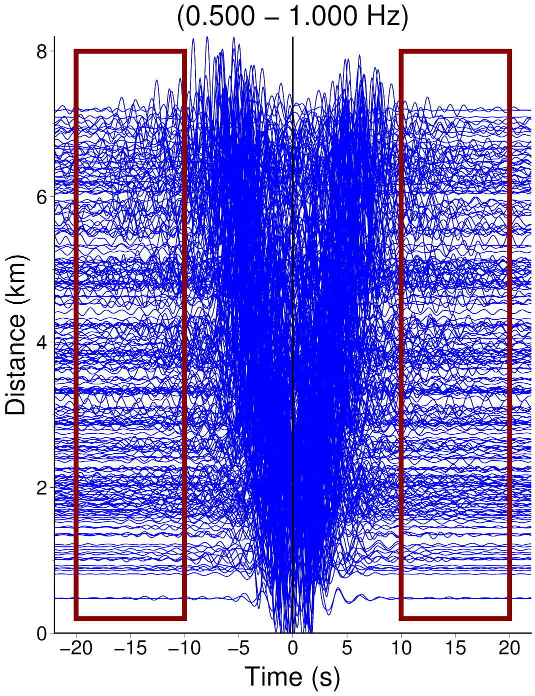

Figure 4: Time-averaged crosscorrelations of recordings of ambient seismic noise associated with station pairs close to the RGS. These $\mathbf{C_{ij}^{(ref)}}$ were filtered between 0.5 and 1.0 Hz. The red boxes indicate the coda window exploited in this study.

$C_{ij}^{(ref)}$ for all station pairs close to the RGS (i.e., including stations from the SIL, ISOR, and REYKJANET networks). The lapse crosscorrelations were compared against the reference crosscorrelation between 10 (t_1) and 20 (t_2) seconds, and for relative velocity increases between $\epsilon = -0.01$ and $\epsilon = 0.01$. Lapse correlation coefficients were computed for the causal and anti-causal parts of the lapse crosscorrelations separately.

4. RESULTS

Figure 5 presents the coda of the causal part of the lapse crosscorrelations between the ambient-noise recordings by stations RET and SDV. The coda appear fairly stable through time. This is corroborated by the lapse CC_{ij}, which are presented in Figure 6 and have values close to 1 (a value of 1 implies equality up to a scale factor) during the entire campaign. Similarly, Figure 6 suggests a high degree of similarity between the coda of the anti-causal parts. It is useful to note that the lapse crosscorrelations are averages of varying numbers of individual crosscorrelations. This is due to gaps in the data and/or a variation over time of the number of events detected by the sta/lta algorithm (see Figure 2).

Figure 7 presents the lapse correlation coefficients and stretching parameters averaged over a number of station pairs. Not all combinations of the nine selected stations (bottom) are taken into account: only station pairs for which the time-averaged lapse correlation coefficient associated with the causal and/or anti-causal part exceeds 0.8 are used. These time-averaged lapse correlation coefficients are denoted by $\overline{CC}_{ij}$. A high value of $\overline{CC}_{ij}$ implies that the coda of the lapse crosscorrelations show, on average, a high degree of similarity to the coda of the reference crosscorrelation. This is a requirement for time-lapse monitoring with ambient-seismic noise and suggests that the background wavefield is sufficiently stable (Obermann *et al.*, 2014, 2015). In case the time-averaged lapse correlation coefficients associated with both causal and anti-causal part exceed 0.8, the lapse CC_{ij} and ϵ_{ij} associated with these two Green's function estimates are averaged prior to being included in the average over different station pairs. Finally, lapse correlation coefficients of individual station pairs are only computed in case $C_{ij}^{(lapse)}$ was computed from more than 50% of the total number of possible time windows. In other words, individual lapse correlation coefficients included in the spatial average presented in Figure 7 are based on $C_{ij}^{(lapse)}$ computed from a minimum of 15 days of data.

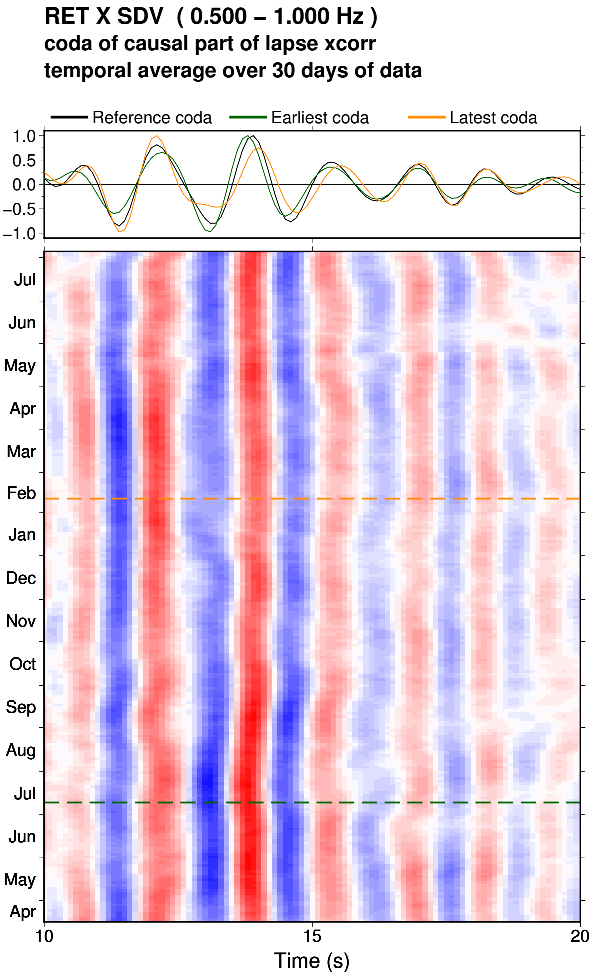

Figure 5: The coda between 10 and 20 seconds of the causal part of the lapse crosscorrelations between station RET and SDV (bottom). Red represents positive values, whereas blue represents negative amplitudes. At the top, the coda of the reference crosscorrelation as well the coda of the lapse crosscorrelations associated with the highest (green) and lowest (orange) ϵ_{ij} are depicted.

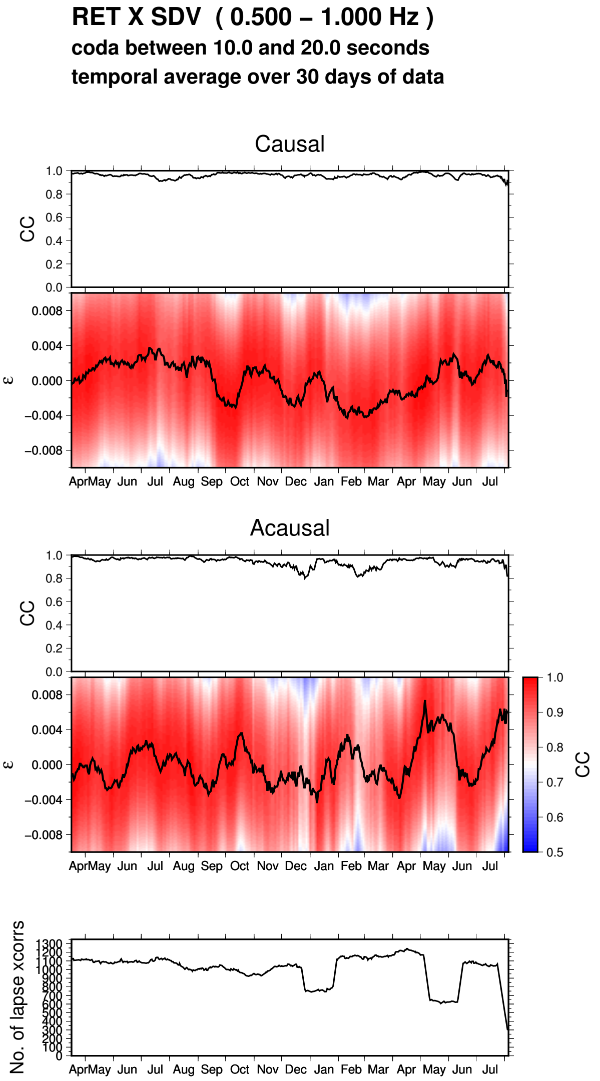

Figure 6: Lapse correlation coefficients, $\mathrm{CC}_{\mathrm{ij}}$, and stretching parameters, ϵ_{ij}, for both the causal and anti-causal coda of the lapse crosscorrelations (black lines). The two contour plots show the correlations coefficients for all values of the stretching parameter, with the black lines tracing the maxima, i.e., the ϵ_{ij}. At the bottom the number of individual crosscorrelations is depicted from which the lapse crosscorrelations are computed, i.e., the number of $\mathrm{C}^{\mathrm{T}}_{\mathrm{ij}}$, associated with the lapse $\mathrm{CC}_{\mathrm{ij}}$.

5. DISCUSSION & CONCLUSIONS

The spatially-averaged lapse correlation coefficients presented in Figure 7 do not show a clear drop at any point in time. Also the spatially-averaged lapse stretching parameters do not show a clear (relative) sudden increase/decrease. Considering the fact that we track changes in the coda of time-lapse surface-wave responses filtered between 0.5 and 1.0 Hz, one would expect a structural change in the subsurface at an approximate depth of about 1 to 2 kilometer to be apparent in the (spatially-averaged) coda (Obermann *et al.*, 2014, 2015). Ideally, such a change could be related to independent data associated with the RGS. The absence of a clear change in the (spatially-averaged) coda suggests that sharp increases/decreases in injection and/or production rates (Figure 8) do not result in a significant structural and/or mechanical change in the medium. This, however, can not be concluded from these results only. First, the parameter space has not been fully explored yet. For example, instead of using $t_1 = 10$ and $t_2 = 20$ different coda windows can be exploited: earlier (later) coda windows are sensitive to changes closer to (further away from) a receiver couple (Pacheco and Snieder, 2005). Also, surface-wave coda at higher (lower) frequencies are sensitive to changes at smaller (larger) depth (Obermann *et al.*, 2013). It may therefore be that at other frequencies there actually is a measurable effect of (potential) structural subsurface changes on the coda. More research (and computing power) is required to investigate this.

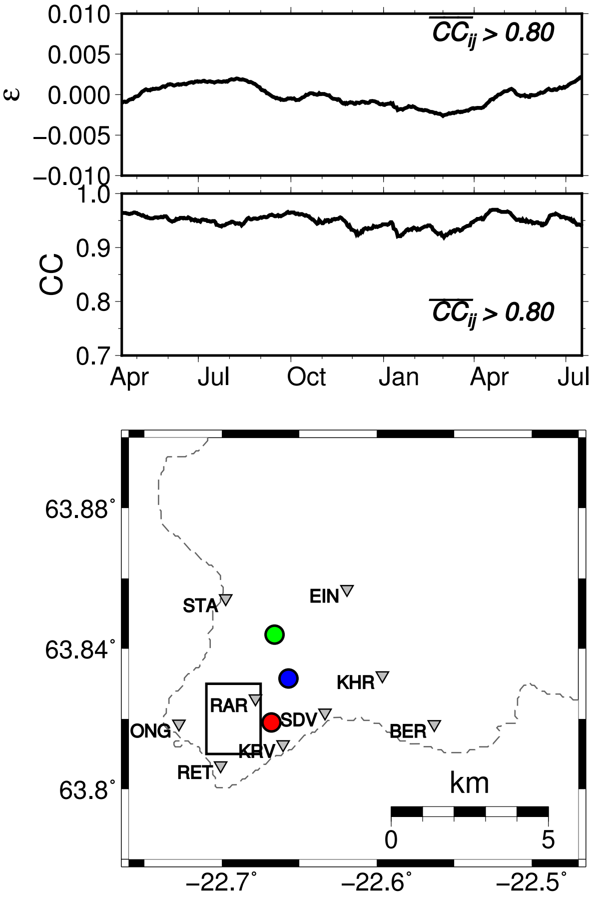

Figure 7: Average lapse stretching parameter and correlation coefficient obtained by averaging over all lapse ϵ_{ij} and $\mathrm{CC_{ij}}$ for which the causal or anti-causal (or both) time-averaged lapse correlation coefficient exceeds 0.8. At the bottom the locations of the seismic stations are depicted (inverted triangles) as well as the approximate location of the production area of the RGS (black square) and the location of three injection wells RN-20B (red), RN-33 (blue), and RN-34 (green).

Second, the source location(s) of the recorded ambient-seismic surface waves varies with time. Although we try to mitigate this effect by discarding time windows containing strong events and averaging the lapse cross-correlations over a period of thirty days, the temporal variation of the coda of individual lapse crosscorrelations (e.g., Figure 5) suggest that some illumination-related changes in the coda remain. The fact that both the lapse correlation coefficient and the lapse stretching parameter do not show the same pattern for the anti-causal part as for the causal part (Figure 6), confirm this. A constant illumination pattern would have resulted in a coinciding temporal behavior of the causal and anti-causal coda, which would only be attributable to changes in the medium. The fact that the RGS is located on the tip of the Reykjanes peninsula implies that, compared to similar studies (e.g., Obermann *et al.*, 2014, 2015), the microseisms exploited in this study are generated relatively close to the area under investigation. Simple geometrical considerations suggest that this proximity may cause the ambient-seismic surface-wave illumination to vary stronger with time than it would at locations further away from the oceans. To confirm this, however, more research is needed.

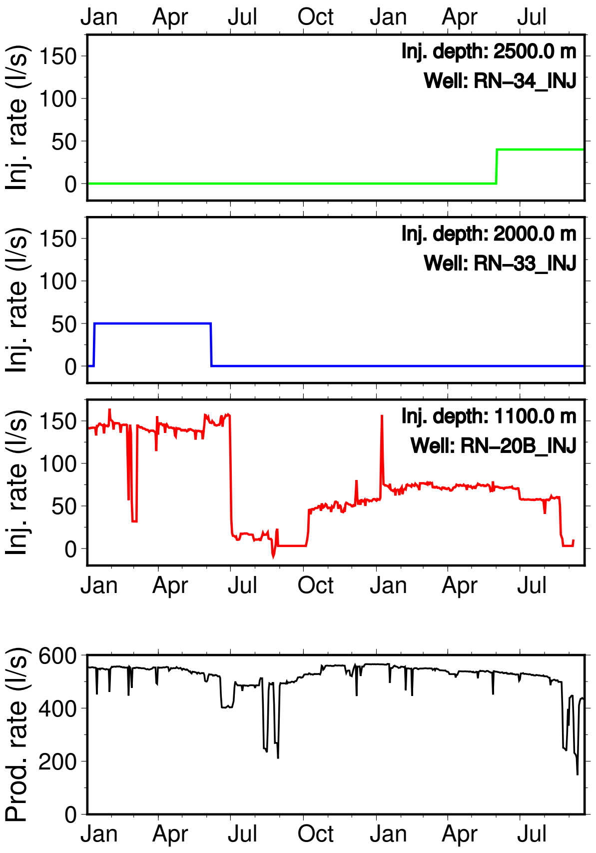

Figure 8: Production rate (bottom) of the RGS (all production wells combined) as well as the injection rates (top) at the three injection wells depicted in Figure 7. The injection in wells RN-34 and RN-33 was for the purpose of a tracer test and the actual rate may have deviated slightly from the (constant) rate given in the graphs.

REFERENCES

Aki, K. Space and time spectra of stationary stochastic waves, with special reference to microtremors. *Bulletin of the Earthquake Research Institute, University of Tokyo*, **35**, (1957), 415–457.

Axelsson, G., Arnaldsson, A., Berthet, J.-c. C., Bromley, C. J., Gudnason, E. Á., Hreinsdóttir, S., Karlsdóttir, R., Magnússon, I. T., Michalczewska, K. L., Sigmundsson, F. and Sigurdsson, O. Renewability Assessment of the Reykjanes Geothermal System , SW-Iceland. In *Proceedings World Geothermal Congress*, page 10 (2015).

Bakulin, A. and Calvert, R. The virtual source method: Theory and case study. *Geophysics*, **71**(4), (2006), SI139–SI150.

Boschi, L. and Weemstra, C. Stationary-phase integrals in the cross-correlation of ambient noise. *Reviews of Geophysics*, **53**, (2015), 411–451.

Bromirski, P. D., Duennebier, F. K. and Stephen, R. A. Mid-ocean microseisms. *Geochemistry, Geophysics, Geosystems*, **6**(4).

Campillo, M. and Paul, A. Long-Range Correlations in the Diffuse Seismic Coda. *Science*, **299**(5606), (2003), 547–549.

Claerbout, J. F. Synthesis of a layered medium from its acoustic transmission response. *Geophysics*, **33**(2), (1968), 264–269.

Draganov, D., Campman, X., Thorbecke, J., Verdel, A. and Wapenaar, K. Reflection images from ambient seismic noise. *Geophysics*, **74**(5), (2009), A63–A67.

Duvall, T. L., Jefferies, S. M., Harvey, J. W. and Pomerantz, M. A. Time-distance helioseismology. *Nature*, **362**(6419), (1993), 430–432.

Fricke, J. T., Evers, L. G., Smets, P. S. M., Wapenaar, K. and Simons, D. G. Infrasonic interferometry applied to microbaroms observed at the Large Aperture Infrasound Array in the Netherlands. *Journal of Geophysical Research: Atmospheres*, **119**(16), (2014), 9654–9665.

Hadziioannou, C., Larose, E., Coutant, O., Roux, P. and Campillo, M. Stability of monitoring weak changes in multiply scattering media with ambient noise correlation: laboratory experiments. *The Journal of the Acoustical Society of America*, **125**(6), (2009), 3688–95.

Halliday, D. and Curtis, A. Seismic interferometry, surface waves and source distribution. *Geophysical Journal International*, **175**(3), (2008), 1067–1087.

Hanasoge, S. M. The influence of noise sources on cross-correlation amplitudes. *Geophysical Journal International*, **192**(1), (2013), 295–309.

Haney, M. M. Infrasonic ambient noise interferometry from correlations of microbaroms. *Geophysical Research Letters*, **36**(19), (2009), L19808.

Hasselmann, K. A statistical analysis of the generation of microseisms. *Reviews of Geophysics*, **1**(2), (1963), 177–210.

Hillers, G., Husen, S., Obermann, A., Planès, T., Larose, E. and Campillo, M. Noise-based monitoring and imaging of aseismic transient deformation induced by the 2006 Basel reservoir stimulation. *Geophysics*, **80**(4), (2015), KS51–KS68.

International Energy Agency (IEA). Medium-Term Renewable Energy Market Report 2015. Technical report, Paris (2015).

Kedar, S., Longuet-Higgins, M., Webb, F., Graham, N., Clayton, R. and Jones, C. The Origin of Deep Ocean Microseisms in the North Atlantic Ocean. *Proceedings of the Royal Society A*, **464**(2091), (2008), 777–793.

Kimman, W. P. and Trampert, J. Approximations in seismic interferometry and their effects on surface waves. *Geophysical Journal International*, **182**(1), (2010), 461–476.

Kohler, M. D., Heaton, T. H. and Bradford, S. C. Propagating Waves in the Steel, Moment-Frame Factor Building Recorded during Earthquakes. *Bulletin of the Seismological Society of America*, **97**(4), (2007), 1334–1345.

Lehujeur, M., Vergne, J., Schmittbuhl, J. and Maggi, A. Characterization of ambient seismic noise near a deep geothermal reservoir and implications for interferometric methods: a case study in northern Alsace, France. *Geothermal Energy*, **3**.

Lobkis, O. I. and Weaver, R. L. Coda-Wave Interferometry in Finite Solids : Recovery of P -to- S Conversion Rates in an Elastodynamic Billiard. *Physical Review Letters*, **90**(25), (2003), 254302.

Longuet-Higgins, M. S. A Theory of the Origin of Microseisms. *Philosophical Transactions of the Royal Society of London. Series A, Mathematical and Physical Sciences*, **243**(857), (1950), 1–35.

McNamara, D. E. and Buland, R. P. Ambient Noise Levels in the Continental United States. *Bulletin of the Seismological Society of America*, **94**(4), (2004), 1517–1527.

Mulargia, F. The seismic noise wavefield is not diffuse. *The Journal of the Acoustical Society of America*, **131**(4), (2012), 2853.

Obermann, A., Froment, B., Campillo, M., Larose, E., Planès, T., Valette, B., Chen, J. H. and Liu, Q. Y. Seismic noise correlations to image structural and mechanical changes associated with the Mw 7.9 2008 Wenchuan earthquake. *Journal of Geophysical Research: Solid Earth*, **119**(4), (2014), 3155–3168.

Obermann, A., Kraft, T., Larose, E. and Wiemer, S. Potential of ambient seismic noise techniques to monitor the St. Gallen geothermal site (Switzerland). *Journal of Geophysical Research B: Solid Earth*, **120**, (2015), 4301–4316.

Obermann, a., Planes, T., Larose, E., Sens-Schonfelder, C. and Campillo, M. Depth sensitivity of seismic coda waves to velocity perturbations in an elastic heterogeneous medium. *Geophysical Journal International*, **194**, (2013), 372–382.

Pacheco, C. and Snieder, R. Time-lapse travel time change of multiply scattered acoustic waves. *The Journal of the Acoustical Society of America*, **118**(3), (2005), 1300.

Poupinet, G., Ellsworth, W. and Frechet, J. Monitoring velocity variations in the crust using earthquake doublets: an application to the Calaveras fault, California (1984).

Roux, P. and Fink, M. Green's function estimation using secondary sources in a shallow water environment. *The Journal of the Acoustical Society of America*, **113**(3), (2003), 1406–1416.

Schuster, G. T., Yu, J., Sheng, J. and Rickett, J. Interferometric/daylight seismic imaging. *Geophysical Journal International*, **157**(2), (2004), 838–852.

Seats, K. J., Lawrence, J. F. and Prieto, G. A. Improved ambient noise correlation functions using Welch's method. *Geophysical Journal International*, **188**(2), (2012), 513–523.

Sens-Schönfelder, C. and Wegler, U. Passive image interferemetry and seasonal variations of seismic velocities at Merapi Volcano, Indonesia. *Geophysical Research Letters*, **33**(21), (2006), 1–5.

Sens-Schönfelder, C. and Wegler, U. Passive image interferometry for monitoring crustal changes with ambient seismic noise. *Comptes Rendus Geoscience*, **343**(8–9), (2011), 639–651.

Shapiro, N. M., Campillo, M., Stehly, L. and Ritzwoller, M. H. High-Resolution Surface-Wave Tomography from Ambient Seismic Noise. *Science*, **307**(5715), (2005), 1615–1618.

Snieder, R., Grêt, A., Douma, H. and Scales, J. Coda wave interferometry for estimating nonlinear behavior in seismic velocity. *Science (New York, N.Y.)*, **295**(5563), (2002), 2253–5.

Snieder, R., van Wijk, K., Haney, M. and Calvert, R. Cancellation of spurious arrivals in Green's function extraction and the generalized optical theorem. *Physical Review E*, **78**(3), (2008), 36606.

Snieder, R. and Şafak, E. Extracting the Building Response Using Seismic Interferometry: Theory and Application to the Millikan Library in Pasadena, California. *Bulletin of the Seismological Society of America*, **96**(2), (2006), 586–598.

Stähler, S. C., Sens-Schönfelder, C. and Niederleithinger, E. Monitoring stress changes in a concrete bridge with coda wave interferometry. *The Journal of the Acoustical Society of America*, **129**(4), (2011), 1945–1952.

Stehly, L., Campillo, M. and Shapiro, N. M. A study of the seismic noise from its long-range correlation properties. *Journal of Geophysical Research*, **111**(B10), (2006), B10306.

Stehly, L., Campillo, M. and Shapiro, N. M. Traveltime measurements from noise correlation: Stability and detection of instrumental time-shifts. *Geophysical Journal International*, **171**(1), (2007), 223–230.

Tsai, V. C. On establishing the accuracy of noise tomography travel-time measurements in a realistic medium. *Geophysical Journal International*, **178**(3), (2009), 1555–1564.

Wapenaar, K. and Fokkema, J. Green's function representations for seismic interferometry. *Geophysics*, **71**(4), (2006), SI33–SI46.

Weaver, R., Froment, B. and Campillo, M. On the correlation of non-isotropically distributed ballistic scalar diffuse waves. *The Journal of the Acoustical Society of America*, **126**, (2009), 1817–1826.

Weemstra, C., Boschi, L., Goertz, A. and Artman, B. Seismic attenuation from recordings of ambient noise. *Geophysics*, **78**(1), (2013), Q1–Q14.

Weemstra, C., Westra, W., Snieder, R. and Boschi, L. On estimating attenuation from the amplitude of the spectrally whitened ambient seismic field. *Geophysical Journal International*, **197**, (2014), 1770–1788.

Wessel, P. and Smith, W. Free software helps map and display data. *EOS Transactions*, **72**, (1991), 441–446.

Withers, M., Aster, R., Young, C., Beiriger, J., Moore, S. and Trujillo, J. A Comparison of Select Trigger Algorithms for Automated Global Seismic Phase and Event Detection. **88**(1), (1998), 95–106.

Woolfe, K. F., Lani, S., Sabra, K. G. and Kuperman, W. Monitoring deep-ocean temperatures using acoustic ambient noise. *Geophysical Research Letters*, **42**, (2015), 2878–2884.

Zhan, Z., Ni, S., Helmberger, D. V. and Clayton, R. W. Retrieval of Moho-reflected shear wave arrivals from ambient seismic noise. *Geophysical Journal International*, **182**(1), (2010), 408–420.

Acknowledgements

C.W. is supported by the Netherlands Research Centre for Integrated Solid Earth Sciences (ISES). We are grateful to the institute of geophysics of the Czech acadamy of sciences (CAS) for using the data recorded by the REYKJANET stations. Similarly, we thank the Icelandic meteorological office (MET office) for allowing us to use their data (SIL network). Instruments for the IMAGE project were provided by the GIPP (Geophysical Instrument pool Potsdam) and the DEPAS (German instrument pool for amphibian seismology). The research leading to these results has received funding from the European Community's Seventh Framework Programme under grant agreement No. 608553 (Project IMAGE). Figures were generated with the help of Generic Mapping Tools (Wessel and Smith, 1991).